

## Experimental and numerical studies of an eastward jet over topography

By YUDONG TIAN<sup>1</sup>, ERIC R. WEEKS<sup>2</sup>†, KAYO IDE<sup>1</sup>,  
J. S. URBACH<sup>2</sup>‡, CHARLES N. BAROUD<sup>2</sup>,  
MICHAEL GHIL<sup>1</sup>¶ AND HARRY L. SWINNEY<sup>2</sup>

<sup>1</sup>Department of Atmospheric Sciences and Institute of Geophysics and Planetary Physics,  
University of California, Los Angeles, CA 90095, USA

<sup>2</sup>Center for Nonlinear Dynamics and Department of Physics, University of Texas at Austin,  
Austin, TX 78712, USA

(Received 8 October 1999 and in revised form 24 October 2000)

Motivated by the phenomena of blocked and zonal flows in Earth's atmosphere, we conducted laboratory experiments and numerical simulations to study the dynamics of an eastward jet flowing over wavenumber-two topography. The laboratory experiments studied the dynamical behaviour of the flow in a barotropic rotating annulus as a function of the experimental Rossby and Ekman numbers. Two distinct flow patterns, resembling blocked and zonal flows in the atmosphere, were observed to persist for long time intervals.

Earlier model studies had suggested that the atmosphere's normally upstream-propagating Rossby waves can resonantly lock to the underlying topography, and that this topographic resonance separates zonal from blocked flows. In the annulus, the zonal flows did indeed have super-resonant mean zonal velocities, while the blocked flows appear subresonant. Low-frequency variability, periodic or irregular, was present in the measured time series of azimuthal velocity in the blocked regime, with dominant periodicities in the range of 6–25 annulus rotations. Oscillations have also been detected in zonal states, with smaller amplitude and similar frequency. In addition, over a large region of parameter space the two flow states exhibited spontaneous, intermittent transitions from the one to the other.

We numerically simulated the laboratory flow geometry in a quasi-geostrophic barotropic model over a similar range of parameters. Both flow regimes, blocked and zonal, were reproduced in the simulations, with similar spatial and temporal characteristics, including the low-frequency oscillations associated with the blocked flow. The blocked and zonal flow patterns are present over wide ranges of forcing, topographic height, and bottom friction. For a significant portion of parameter space, both model flows are stable. Depending on the initial state, either the blocked or the zonal flow is obtained and persists indefinitely, showing the existence of multiple equilibria.

---

† Present address: Physics Department, Emory University, Atlanta, GA 30322, USA.

‡ Present address: Department of Physics, Georgetown University, Washington, DC 20057, USA.

¶ Author to whom correspondence should be addressed.

## 1. Introduction and motivation

The interaction of rotating flows with underlying topography is a classic topic of geophysical fluid dynamics (Gill 1982; Pedlosky 1987). Various applications to the atmosphere of Earth (Charney & Eliassen 1949; Bolin 1950), Mars (Keppen & Ingersoll 1995) and Jupiter (Dowling & Ingersoll 1989), as well as to Earth's oceans (Holloway 1992) have been worked out. We are motivated here primarily by the potential role of such interactions in the Earth atmosphere's low-frequency variability, but expect some of our results to also apply to other areas of geophysical fluid dynamics.

Because of its important role in the understanding of the general circulation of the atmosphere and in extended-range weather forecasting, low-frequency variability of large-scale atmospheric flows has been documented and studied for over fifty years. In particular, since the late 1930s meteorologists have recognized that the large-scale flow in the Northern Hemisphere alternates between two distinct states, called high-index and low-index flows; the former is characterized by a zonally straight and faster jet stream and the latter by a wavier and slower one. Such an oscillation tends to have a more or less regular cycle of 4–6 weeks, and is called the index cycle (Rossby 1939; Namias 1950; Webster & Keller 1975). Blocking (Rex 1950*a, b*) plays an important role in low-index flows; it involves a strong high-pressure ridge that appears at preferred locations mostly during the winter, and blocks the normally zonal flow. A regional block can last for 10–30 days, with substantial impact on large-scale weather patterns (O'Connor 1963; Weeks *et al.* 1997).

During the 1970s and 1980s, subtler low-frequency atmospheric phenomena were discovered and studied extensively. Among them are the low-frequency oscillations with periods of 40–50 days, which were first detected in tropical convection and zonal winds (Madden & Julian 1971, 1972), and were also found later by analysis of length-of-day and atmospheric angular momentum data (Langley, King & Shapiro 1981). More detailed observational studies (Anderson & Rosen 1983; Dickey, Ghil & Marcus 1991) have identified a significant contribution to such oscillations from the Northern Hemisphere extratropics.

Considerable efforts have been devoted to studying the dynamics of these low-frequency phenomena and their underlying relationships. In a barotropic model, Charney & DeVore (1979) obtained multiple equilibria resulting from the nonlinear interactions between large-scale mid-latitude flow and the underlying topography. The two stable states so obtained had certain features in common with blocked and zonal, or low-index and high-index states in the atmosphere (Charney & Straus 1980; Charney, Shukla & Mo 1981). Subsequent studies using various analytical and numerical models (e.g. Hart 1979; Pedlosky 1981; Legras & Ghil 1985; Yoden 1985; Ghil & Childress 1987, Chap. 6) yielded either multiple equilibria or multiple flow regimes, and highlighted the role of topography in the dynamics of such flows. Some of these studies also obtained low-frequency oscillations, associated with one or all of the stationary flow solutions (Charney & DeVore 1979; Legras & Ghil 1985; Yoden 1985; Ghil 1987; Strong, Jin & Ghil 1993), and speculated that such oscillations may be related to the 40–50-day oscillations observed in the Northern Hemisphere extratropics (Ghil & Mo 1991).

Laboratory studies that model atmospheric phenomena have also played an important role in our understanding of planetary-flow dynamics since the early stages of the atmospheric sciences. Several rotating annulus experiments have previously investigated the index cycle, blocking, and low-frequency oscillations (Pfeffer & Chiang

1967; Li, Kung & Pfeffer 1986; Pfeffer, Kung & Li 1989; Bernardet *et al.* 1990; Jonas 1981; Pfeffer *et al.* 1990). Introducing wavenumber-two topography in such annuli produced new phenomena, such as large-scale standing waves and low-frequency vacillations associated with them, but did not adequately explain the spatio-temporal features of the atmosphere's observed and modelled low-frequency variability.

Those experiments used baroclinic annuli with thermal forcing. Low-frequency atmospheric dynamics is, however, predominantly barotropic (Wallace & Blackmon 1983; Marcus, Ghil & Dickey 1994, 1996), and so direct simulation and investigation of barotropic dynamics is desirable for studying those phenomena (Lorenz 1972). Lau & Nath (1987) have shown that the larger the time scale, the more barotropic the flow becomes. Furthermore, the complications that arise from the fully three-dimensional structure of the flows in the baroclinic annuli make the analysis of the experimental results more difficult and hinder direct comparisons with existing theoretical results and atmospheric observations. Finally, because the forcing mechanism in those experiments was through differential heating of the sidewalls, large Reynolds numbers are difficult to achieve and thus the parameter range is limited.

Several barotropic experiments with topography were conducted (Carnevale, Kloosterziel & van Heijst 1991; Pratte & Hart 1991; Pfeffer *et al.* 1993) but did not examine questions of blocking and zonal patterns. Streamfunction fields shown in Pfeffer *et al.* (1993) resemble some of our flow patterns here (see §2), but the Rossby numbers for these experiments were very low and the flows examined were always time-independent. The general theory of rotating flow over topography (Queney 1947; Ghil & Childress 1987; Pedlosky 1987; Smith 1989; Wurtele, Sharman & Datta 1996), on the other hand, suggests topographic effects on barotropic flow could be quite significant and thus lead to multiple equilibria, as well as to time-dependent flows, even in the presence of constant forcing.

In the present paper we report on experimental results obtained for barotropic flow in a rotating annulus; the flow is driven through concentric rings of holes in the bottom, using a mechanical pump. This generates an eastward jet, and we investigate the interactions of this jet with two symmetrically placed mountains on the bottom of the annulus. We observe two distinct flow patterns, analogous to high- and low-index flows in the atmosphere. For moderate to high pumping rates, these flows exhibit low-frequency oscillations, with different oscillatory features being associated with different flows. We also observed spontaneous transitions between these two flow regimes.

The experiment uses a much-simplified laboratory model of Earth's atmosphere. Our fluid is isothermal and incompressible, and the rigid side, top, and bottom walls of our annular container differ from the atmosphere's boundaries. To help understand the laboratory results and connect them with numerical models of the atmosphere (Charney & DeVore 1979; Pedlosky 1981; Legras & Ghil 1985; Jin & Ghil 1990) and with observations (Dickey *et al.* 1991; Ghil & Mo 1991; Lott, Robertson & Ghil 2001), we constructed a numerical model to simulate the annulus experiment. The model is governed by the quasi-geostrophic (QG) barotropic potential vorticity equation (e.g. Charney & DeVore 1979; Marcus & Lee 1998; Pedlosky 1987 Chap. 4), with forcing and mountains similar to those in the experiment. The values of the parameters in the model are derived directly from the laboratory measurements. The flow patterns and time dependence obtained in the model agree qualitatively with those in the experiments, for equivalent parameter values. Furthermore, we use the model to investigate the influence of topographic height and bottom friction on the dynamics, since these parameters are difficult to vary in the laboratory experiments.

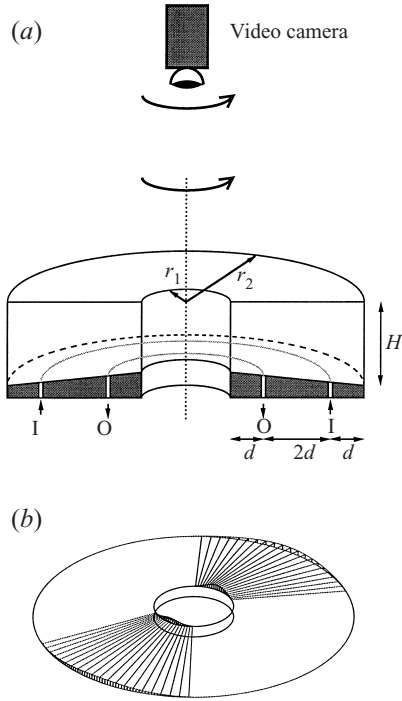


FIGURE 1. (a) The rotating annulus and (b) the bottom topography. The inner radius is  $r_1 = 10.8$  cm and the outer radius is  $r_2 = 43.2$  cm; the depth of the annulus increases from 17.1 cm at  $r_1$  to 20.3 cm at  $r_2$ . The angular extent of each of the two mountains is 1.25 rad. The arrows below the tank in (a) show the direction of the inflow (I) and outflow (O) through the holes in the bottom. See text for other details.

The experimental results of this research are presented in §2. The numerical investigation is reported in §3. In §4 we summarize the results and compare the laboratory results and the computer simulations, and discuss the implications for Earth's atmosphere.

## 2. Experimental investigation

### 2.1. Apparatus and experimental design

The experimental apparatus consists of a large rotating annulus, shown schematically in figure 1 (Solomon, Holloway & Swinney 1993; Weeks *et al.* 1997). The top is rigid and flat, and the bottom is rigid and conical with a constant radial slope  $s = 0.1$ , to simulate the  $\beta$ -effect. The tank is filled with water, of kinematic viscosity  $\nu = 0.0090 \text{ cm}^2 \text{ s}^{-1}$ , and can rotate at speeds up to  $\Omega = 8\pi \text{ rad s}^{-1}$ .

Two symmetric, rigid mountains are overlaid on the tank's conical bottom, to simulate the dominant topographic component in Earth's Northern Hemisphere (Charney & Eliassen 1949; Peixoto, Saltzman & Teweles 1964; Legras & Ghil 1985). Above the conical bottom, each mountain has a Gaussian profile along the azimuthal direction, and is flat along the radial direction; thus each mountain's surface is described by

$$h(r, \theta) = h_0 \exp(-\theta^2/\theta_0^2), \quad (2.1)$$

where  $r$  is the radius measured from the centre of the annulus,  $\theta$  is the azimuthal angle measured from the centreline of the mountain,  $h_0 = 1.5$  cm is the maximum height of both mountains, and  $\theta_0 = 0.37$  rad. Each mountain extends over 1.25 rad, and its two radial side edges are smoothly tapered from the Gaussian profile of (2.1) to zero to meet the bottom.

To form a jet in the tank, two concentric rings of small holes were drilled through the bottom and the mountains, located at  $r_{\text{sink}} = 1.75r_1$  and  $r_{\text{source}} = 3.25r_1$ . These forcing rings each have 120 holes of 0.26 cm in diameter. A pump forces fluid into the tank at the outer ring and removes fluid at the inner ring at a constant flow rate  $F$ . Due to the counter-clockwise rotation of the annulus, the action of the Coriolis force deflects the otherwise radial flow into a co-rotating, ‘eastward’ jet.

To observe the flows obtained in the experiment, we use a particle-tracking technique due to Pervez & Solomon (1994). Neutrally buoyant particles, 1.0 mm in diameter, are added to the fluid. A 2 cm tall horizontal layer of fluid at the tank’s mid-depth is illuminated from the side, and viewed from a co-rotating video camera above the experiment. The images from the video camera are stored in a computer, post-processed to track individual particles, and the time-averaged velocity field is extracted from these data. The corresponding streamfunction field is calculated by a least-squares technique that uses 9 spectral modes in the radial direction and 43 spectral modes in the azimuthal direction.

Additionally, to collect more precise information about the velocity fluctuations, we use two hot-film probes. These two probes are placed inside the tank at the same horizontal position, shown in figure 2, at the channel’s mid-radius,  $r = 2.5r_1$ , about  $15^\circ$  upstream of one of the mountains. The sensors are oriented to measure the azimuthal component of the flow velocity, and one is placed approximately 1 cm below the top lid and the other 1 cm above the bottom. This allows us to examine the vertical structure of the flow at this horizontal position, and confirm its predominantly two-dimensional, barotropic character.

We explored the flows over a wide range of parameters. For each combination of parameter values, we carried out several runs with different initial states.

## 2.2. Experimental results

### 2.2.1. Control parameters and two-dimensionality of the flow

We have two independent control parameters, the forcing flow rate  $F$  and the angular velocity  $\Omega$  of the tank: the pump flux rate  $F$  ranges from 0 to  $400 \text{ cm}^3 \text{ s}^{-1}$ , the rotation rate  $\Omega$  from  $1.5\pi$  to  $3\pi \text{ rad s}^{-1}$ . The forcing is measured by a non-dimensional Rossby number, given by

$$Ro = \frac{U}{fL}, \quad (2.2)$$

where  $L$  is the spacing between the forcing rings,  $L = r_{\text{source}} - r_{\text{sink}} = 1.5r_1 = 16.2$  cm;  $U$  is the characteristic velocity of the flow; and  $f = 2\Omega$  is the Coriolis parameter. The actual velocity of the fluid depends, of course, on the flow regime. Previously (Weeks *et al.* 1997), we chose  $U$  to be the maximum velocity that would result from a steady, axisymmetric flow in the absence of topography (Legras & Ghil 1985; Sommeria, Meyers & Swinney 1991),

$$U_{\text{max}} = (F/2\pi)(\Omega/\nu)^{1/2}r_{\text{sink}}^{-1}. \quad (2.3)$$

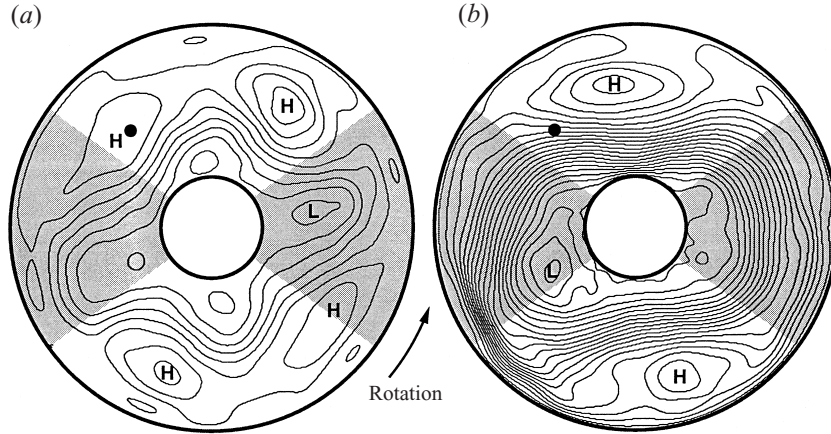


FIGURE 2. Time-averaged streamfunction field for (a) blocked and (b) zonal flow. The streamfunction is calculated from the velocity field measured by particle tracking. The shaded areas indicate the coverage of the mountains, and the black dot indicates the position of the hot-film probes. The contour interval is  $15 \text{ cm}^2 \text{ s}^{-1}$  for both streamfunctions, and the letters H and L indicate the highs and lows of the streamfunctions. The Rossby numbers  $Ro$  for the blocked and zonal flows are  $0.044 \pm 0.004$  and  $0.066 \pm 0.004$  respectively (pump flux  $F = 260$  and  $390 \text{ cm}^3 \text{ s}^{-1}$ ); for both flows, the Ekman number is  $Ek = 4.8 \times 10^{-4}$  ( $\Omega = 3\pi \text{ rad s}^{-1}$ ).

However, Legras & Ghil (1985) pointed out that  $U_{\max}$  overestimates the actual velocity  $U$  (see also figures 3 and 4 here), so we use  $U = U_{\max}/5$  in the current paper. The scaling factor  $1/5$  is chosen to give values of  $U$  that are close to the observed flow velocity in the presence of the topography.

The second non-dimensional number we use is the Ekman number, given by

$$Ek = \left( \frac{T_{\text{annulus}}}{T_{\text{Ekman}}} \right)^2 = \left( \frac{4\pi}{H} \right)^2 \left( \frac{\nu}{\Omega} \right), \quad (2.4)$$

where  $H$  is the mean depth of the tank (18.7 cm),  $T_{\text{annulus}} = 2\pi/\Omega$  is the annulus rotation period, and  $T_{\text{Ekman}} = H/2(\nu\Omega)^{1/2}$  is the relaxation time for unforced disturbances (Sommeria *et al.* 1991). Note that  $Ek$ , unlike  $Ro$ , does not depend on the forcing  $F$ , while both depend on the rotation rate  $\Omega$  ( $Ro \sim \Omega^{-1/2}$  and  $Ek \sim \Omega^{-1}$ ).

Since the annulus rotates rapidly and the forcing is relatively weak, the two non-dimensional control parameters are small for our experiments:  $0.003 < Ro < 0.100$  and  $10^{-4} < Ek < 10^{-3}$ . Because of this, the flow velocities in the annulus are predominantly two-dimensional and depend mostly on horizontal position. This essentially barotropic character of the flow is a result of the Taylor–Proudman theorem for rapidly rotating fluids (Greenspan 1968).

We verified the flow's barotropic nature by examining separately the velocity signals as measured individually by the two hot-film probes, mounted at the same horizontal position but at the top and bottom of the tank. The correlation coefficient between the two velocity signals is typically above 0.9 for all the experiments conducted. In the results discussed in this section, the time series displayed were obtained from the top probe; signals from the bottom probe (not shown) were similar.

### 2.2.2. Blocked and zonal flow patterns

We obtained two distinct types of flows in the experiments, by varying the control parameters in the  $(F, \Omega)$ -plane and by testing various initial states. Figure 2 shows

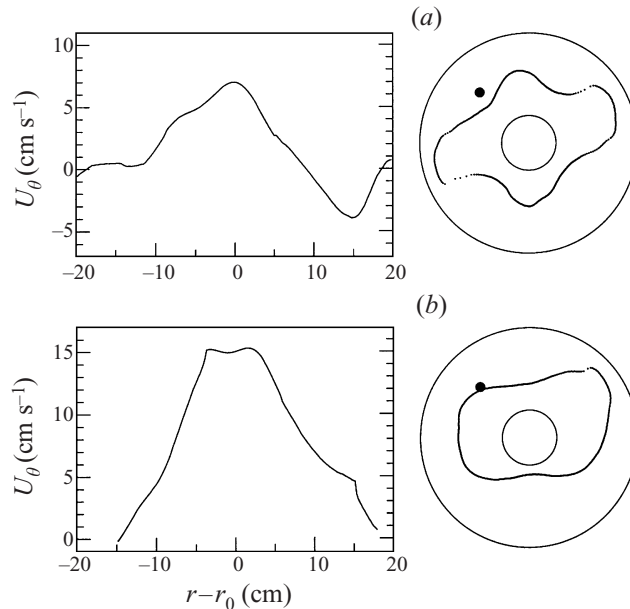


FIGURE 3. Time- and azimuthally-averaged azimuthal velocity profile (left-hand panels), relative to the axis of the jet, for (a) blocked and (b) zonal flow. The streamfunction contour giving the approximate position of the jet axis as  $r_0 = r_0(\theta)$  is indicated in the corresponding right-hand panels; the data are shifted relative to this  $r_0$  for a given value of  $\theta$  and then averaged azimuthally (the black dot indicates the position of the hot-film probe). The data correspond to the streamfunctions shown in figure 2. The velocity profiles obtained are similar for other contour choices (except for a radial offset).

time-averaged streamfunction patterns characteristic of these two types. At low  $Ro$  (lower forcing or higher rotation), the co-rotating jet is weak and wavy (figure 2a). At higher  $Ro$  (higher forcing or lower rotation), we observe a flow pattern that is quite different (figure 2b) with the co-rotating jet much more rapid and less meandering. In an intermediate range of  $Ro$  values, both flow types exist and will be described in §2.2.4.

If we consider that our annulus flows are idealized models of Northern Hemisphere mid-latitude flows, the azimuthal velocity in the tank corresponds to the zonal wind component in the atmosphere. A counter-clockwise or co-rotating jet in the tank thus corresponds to an eastward or 'westerly' jet in the atmosphere. Accordingly, it is natural to associate the low- $Ro$  flow in the annulus with blocked or low-index flow in the atmosphere and the high- $Ro$  flow with zonal or high-index flow (Rossby 1939; Namias 1950; Charney & DeVore 1979; Ghil & Childress 1987, Chaps. 5 and 6). For simplicity, we shall refer henceforth to low- $Ro$  flow regime in the annulus as *blocked*, and to the high- $Ro$  flow as *zonal*.

The spatial features of the two flow regimes indicate clearly that the effect of long-wave bottom topography on large-scale rotating flow is much more pronounced at lower  $Ro$ , at which the topography both deflects and slows down the flow appreciably. Both blocked and zonal flow patterns have a strong wavenumber-two component in the zonal direction, and their phases relative to the mountains are largely fixed. Under similar conditions in the absence of topography, by contrast, upstream-propagating Rossby waves are observed and no flow features are fixed relative to the annulus (Sommeria *et al.* 1989, 1991; Solomon *et al.* 1993).

The azimuthal flux carried by the zonal flows is typically 3 times larger than in the blocked case for the same pumping and rotation rates (not shown). The blocked flow shown in figure 2 ( $Ro = 0.044 \pm 0.004$ ) has a net average azimuthal flux of  $1100 \text{ cm}^3 \text{ s}^{-1}$ , while the zonal flow shown ( $Ro = 0.066 \pm 0.004$ ) has a net azimuthal flux of  $4900 \text{ cm}^3 \text{ s}^{-1}$ , over 400% larger, despite the change in forcing of only 50%. This is evidence of the fairly abrupt, nonlinear drop in topographic effects as  $Ro$  increases (Held 1983).

The azimuthal velocity profile for blocked and zonal flow is shown in figures 3(a) and 3(b), respectively. The zonal jet appears slightly narrower and has a steeper velocity gradient on its flanks.

The jet is deflected to form a stationary Rossby wave when it flows over the topography. Linear theory predicts that there is an optimal jet velocity  $U_r$  at which the jet will experience maximum deflection, due to resonance with the periodic topography. The large difference in jet velocity between the two types of flow suggests that the zonal flow and the blocked flow are on opposite sides of the topographic resonance. For a topography with wavenumbers  $(k_x, k_y)$ , the jet velocity  $U_r$  which is linearly resonant with it (Egger 1978; Ghil & Childress 1987, §6.2; Pfeffer *et al.* 1993) is given in the quasi-geostrophic approximation by

$$U_r = \beta / (k_x^2 + k_y^2), \quad (2.5)$$

where

$$\beta = 2\Omega s / H; \quad (2.6)$$

in (2.6)  $s = 0.1$  is the slope of the tank's bottom, and  $H = 18.7 \text{ cm}$  the mean depth of the water.

Figure 3(a, b) (left-hand panels) shows that the azimuthally averaged peak jet speeds are about  $7 \text{ cm s}^{-1}$  for the blocked flow shown in figure 2(a), and  $15 \text{ cm s}^{-1}$  for the zonal flow of figure 2(b). For the rotation rate  $\Omega$  used in figure 3, and for our topography that has two waves in the azimuthal direction,  $U_r$  calculated from (2.5) is  $12.7 \text{ cm s}^{-1}$ ; this uses  $k_x = 2/\bar{r}_0$ —where  $\bar{r}_0$  is the mean radial position of the jet,  $\bar{r}_0 = 22.5 \text{ cm}$  (see the right panels of figure 3a, b), so that  $k_x = 0.089 \text{ cm}^{-1}$ —and  $k_y = 0$ . The value of  $U_r$  so obtained indicates that our blocked flow is in a subresonant state, and the zonal flow is in a super-resonant state (cf. Charney & DeVore 1979; Charney *et al.* 1981; Ghil & Childress 1987, §6.3). This resonance is consistent with the two distinct phase relations between the two flow patterns and the topography (figure 2a, b).

Blocked and zonal flows not only show distinct spatial patterns, but also exhibit qualitatively different temporal behaviour. An example appears in figure 4, showing time series of azimuthal velocity for blocked and zonal flow. The blocked flow, shown in panel (a), has a small mean azimuthal velocity of  $5.4 \text{ cm s}^{-1}$ , and exhibits large-amplitude, low-frequency fluctuations. By contrast, the zonal flow in panel (c) has a much larger mean azimuthal velocity, of  $12.0 \text{ cm s}^{-1}$  in this case, but smaller and rapid fluctuations. The resonant velocity  $U_r$  for the rotation rate used in figure 4 is  $6.4 \text{ cm s}^{-1}$ .

Examination of the video and snapshots of the flows (not shown) reveals that the time variability in the blocked flow manifests itself in several kinds of flow pattern changes: the strength and the orientation of the deep troughs on the downstream flanks of the mountains (see figure 2a) undergo large variations with time; the shape and the position of the small cut-off cyclones in the valleys, near the inner wall,

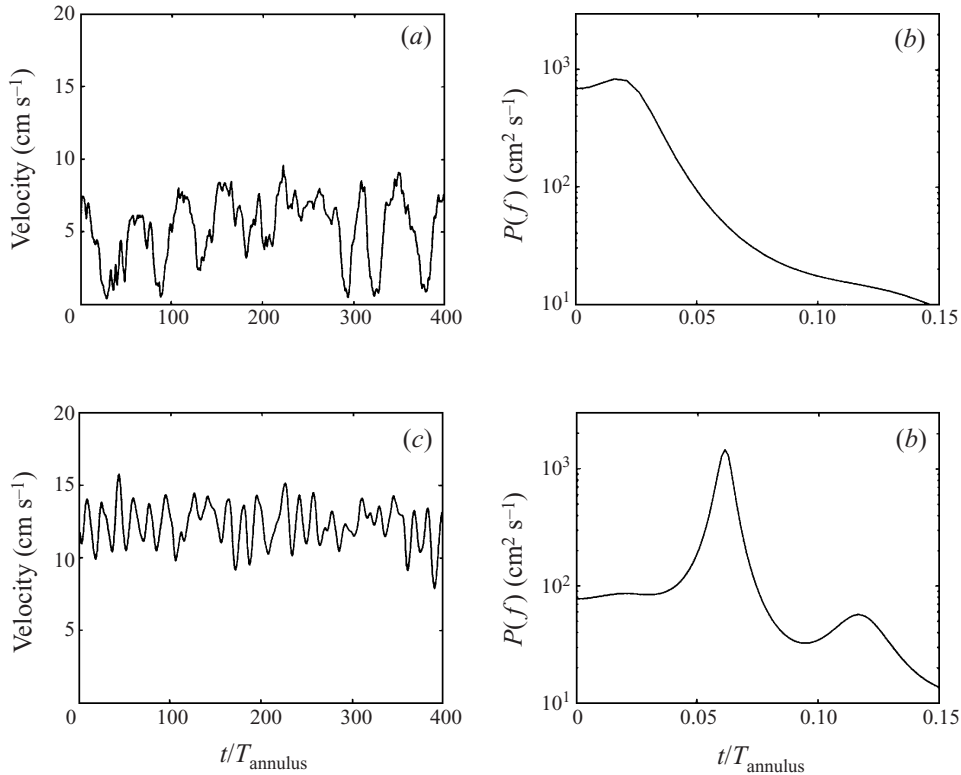


FIGURE 4. Time series of azimuthal velocity, measured by the hot-film probe near the lid (see location in figure 2), for (a) blocked and (c) zonal flow; and power spectra, for (b) blocked and (d) zonal flow. The rotation rate of the annulus is  $\Omega = 1.5\pi \text{ rad s}^{-1}$  for both cases, while the forcing flow rate is  $F = 100$  and  $400 \text{ cm}^3 \text{ s}^{-1}$  for blocked and zonal flows respectively ( $Ek = 9.6 \times 10^{-4}$ ;  $Ro = 0.024 \pm 0.001$  and  $0.096 \pm 0.004$ , respectively).

fluctuate significantly; and the strength of the jet shows considerable change from time to time. The fluctuations in the zonal flow are primarily associated with the slight motions of the cyclone above the downstream half of each mountain, near the inner wall (see figure 2b).

### 2.2.3. Low-frequency oscillations of blocked flows

The low-frequency oscillations in the blocked flows are of particular interest, since Ghil (1987) hypothesized that an oscillatory instability of blocked flow over topography might cause the 40–50-day oscillations in the Northern Hemisphere's mid-latitudes (see also Ghil & Childress 1987, §6.4; Jin & Ghil 1990). In order to see how the characteristics of these oscillations in the annulus are affected by the control parameters, we show several time series of the zonal velocity in figure 5.

The blocked flows become time independent at low  $Ro$  (not shown). Due to difficulties in operating the pump at steady  $F$  for low pump rates, the onset of time dependence could not be cleanly observed. At  $Ro \approx 0.004$  the flow has periodic oscillations, with an oscillation period of about 50 annulus rotation periods (figure 5a). A sequence of barotropic model results using models of Northern Hemisphere flow of increasing detail and sophistication (Legras & Ghil 1985; Jin & Ghil 1990; Strong *et al.* 1993) all obtained oscillations of the flow with periods of 40–50 days via

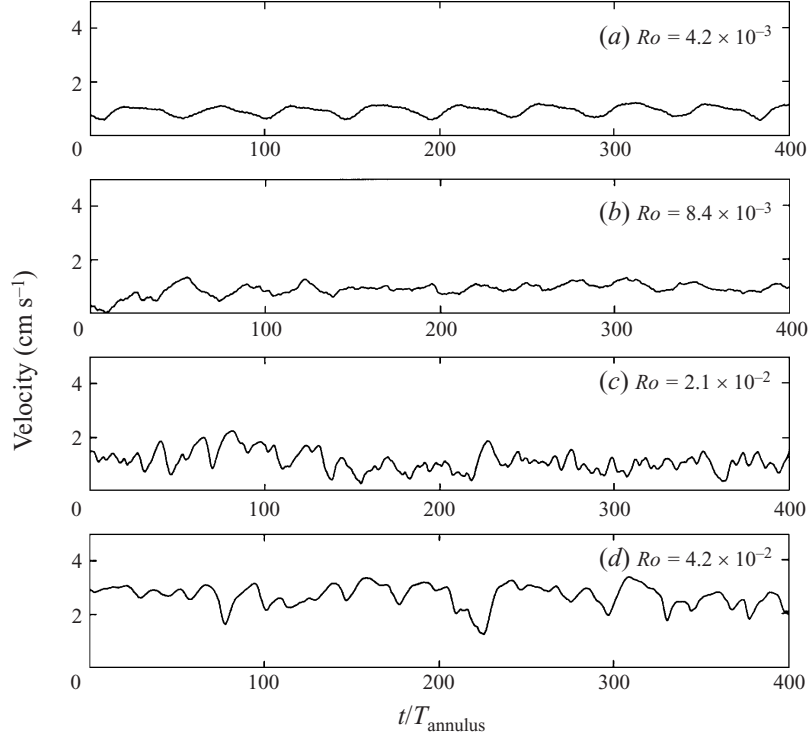


FIGURE 5. Velocity time series from blocked flow at low  $Ro$ . The Rossby numbers for each flow are indicated, with uncertainties  $\pm 5\%$ , and  $Ek = 4.8 \times 10^{-4}$  for all flows ( $\Omega = 3\pi \text{ rad s}^{-1}$ ). For the first time series ( $Ro = 0.0042$ ), the period is  $32 \text{ s} = 48 T_{\text{annulus}}$ . The pump rates for these flows are  $F = 25, 50, 125, \text{ and } 250 \text{ cm}^3 \text{ s}^{-1}$ . Time series for zonal flow at  $Ek = 4.8 \times 10^{-4}$  (not shown) are qualitatively similar to those seen in figure 4(c), which corresponds to zonal flow at  $Ek = 9.6 \times 10^{-4}$ .

Hopf bifurcation of the blocked flow. These results suggest that the low-frequency oscillations seen in figure 5(a) may also be due to a Hopf bifurcation, although this cannot be determined directly from our experiments.

As the forcing is increased (figure 5b–d), the mean flow rate increases, and the fluctuations become more irregular and of higher amplitude. The power spectra of these time series are shown in figure 6. At  $Ro = 0.0042$ , there are pronounced peaks at 50 annulus periods and at the first harmonic of this frequency.

#### 2.2.4. Regime diagram

Figure 7 shows the experiment's phase diagram. For lower forcing  $F$  (lower  $Ro$ ), the blocked state is stable; for higher forcing, the zonal state is stable. As the rotation rate  $\Omega$  of the annulus is increased (lower  $Ek$ ), stronger forcing is necessary to produce a zonal flow. Due to the  $\Omega^{-1/2}$  dependence of  $Ro$ , the pump flux  $F$  needed for zonal flow increases as  $\Omega$  is increased (see (2.2) and (2.3)). This is consistent with the resonance argument. Faster rotation of the tank leads to a larger value of  $\beta$ , cf. (2.6), and consequently, a larger resonance velocity, cf. (2.5); this, in turn, requires a larger jet velocity to achieve super-resonance. On the other hand, when the jet is not strong enough, the flow tends to the subresonant, blocked state.

At intermediate  $Ro$ , either flow pattern can persist for fairly long time intervals. If the run is continued for long enough, however, the flow spontaneously switches

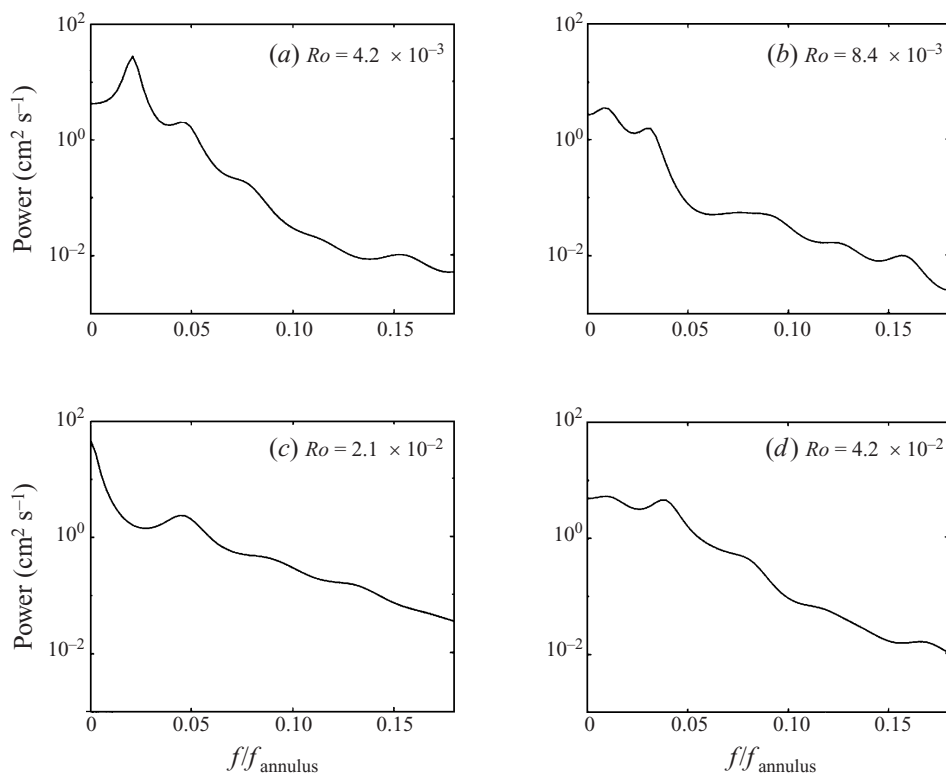


FIGURE 6. Power spectra of the corresponding azimuthal velocity time series shown in figure 5, at  $\Omega = 3\pi \text{ rad s}^{-1}$  ( $Ek = 4.8 \times 10^{-4}$ ) and different values of  $Ro$ . The spectra in this and subsequent figures were obtained using the maximum-entropy method after data-adaptive pre-filtering by singular-spectrum analysis (Dettinger *et al.* 1995).

between blocked and zonal flows. This is shown in figure 8(a), where the distinct signatures of the two flow regimes can be seen. The transitions are clear cut, although they take several annulus rotation periods to be completed (see figure 8b). Such transitions occur at irregular intervals and do not appear predictable.

The time the flow spends in one regime before it switches to the other is quite variable, but is much longer than the oscillation periods of either the zonal or blocked flows: each flow regime usually persists for at least a few hundred annulus rotations, and sometimes thousands, before it switches to the other regime. The alternation between fairly long stays in either regime, on the one hand, and fairly rapid transitions between regimes, on the other, is very similar to that seen in the barotropic model of Legras & Ghil (1985). Weeks *et al.* (1997) described how the percentage of time spent in the blocked regime decreases with Rossby number (see figure 4 there). They also discussed how this result compares with similar properties of observed atmospheric flows (Dole & Gordon 1983) and of flows in a barotropic model on the sphere (Legras & Ghil 1985).

We have carried out selected experiments at higher rotation rates, up to  $\Omega = 6\pi \text{ rad s}^{-1}$ , although not in the detail necessary to extend our phase diagrams (figure 7). Blocked and zonal flow patterns are both present at these higher rotation rates, as well as the spontaneous transitions between them.

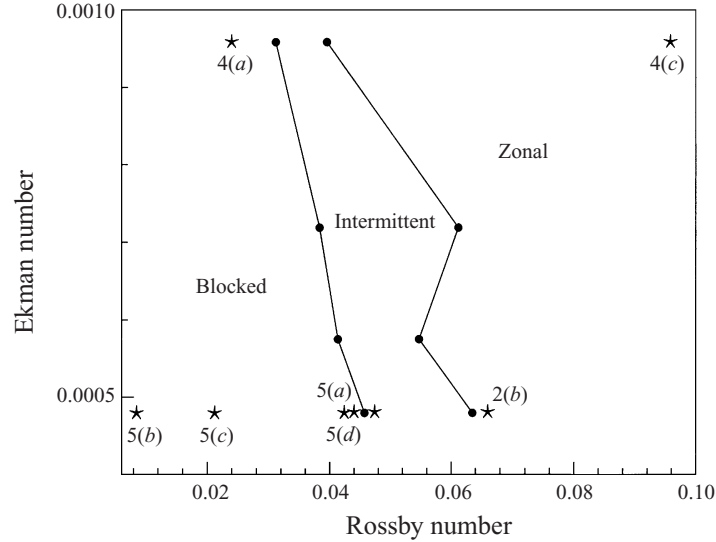


FIGURE 7. Phase diagram showing regions of differing flow patterns in the experiment, as a function of  $Ro$  and  $Ek$ . In each of the two regions labelled ‘Blocked’ and ‘Zonal’, the resulting flows are stable, resemble the pattern associated with the respective label, and occur from any initial state. In the middle region between the two that is labelled ‘Intermittent’, the flow pattern switches spontaneously between the blocked and zonal flows. The black dots at the boundaries of this region are derived from experimental runs at constant  $Ek$  by using the highest and lowest values of  $Ro$  where intermittent behaviour was found (see also figure 4 in Weeks *et al.* 1997). The locations of experimental runs used for figures 2, 4, 5 and 8 are indicated by asterisks.

### 3. Numerical investigation

#### 3.1. Model formulation

##### 3.1.1. Governing equation

Our model is governed by the quasi-geostrophic barotropic potential-vorticity equation, since the flow in the rotating annulus is predominantly two-dimensional and nearly geostrophic, due to the rapid rotation of the annulus. Including vorticity forcing, Ekman friction and eddy viscosity, the dimensional form of the equation is (Ghil & Childress 1987; Pedlosky 1987; Marcus & Lee 1998),

$$\frac{\partial}{\partial t}(\nabla^2\psi) + J(\psi, \nabla^2\psi) + \frac{fs}{H} \frac{\partial\psi}{\partial x} + \frac{f}{H} J(\psi, h) = -\frac{(2A_V f)^{1/2}}{H} \nabla^2(\psi - \psi_*) + \nu \nabla^4(\psi - \psi_*). \quad (3.1)$$

On the left-hand side,  $J$  is the Jacobian operator,  $\psi = \psi(x, y, t)$  is the streamfunction,  $H$  is the mean depth of the fluid,  $f = 2\Omega$  is the Coriolis parameter,  $s$  is the tank’s bottom slope, and  $h = h(x, y)$  is the height of the topography measured from the underlying sloping bottom. We follow Lorenz (1963) in neglecting the curvature of the annular gap in the tank, so that  $x$  corresponds to  $r\theta$  and  $y$  to  $r$ ;  $y$ , however, points toward the axis of rotation or ‘poleward’, in the customary atmospheric analogy.

The right-hand side of (3.1) includes the forcing, Ekman friction and eddy viscosity;  $\psi_* = \psi_*(x, y)$  is the streamfunction of the external forcing field, which produces the eastward jet and whose exact form will be derived further below (see (3.7) and (3.8)). The vertical component  $A_V$  of the turbulent viscosity coefficient in the frictional boundary layers is taken to be the same at the top and bottom (Charney & DeVore

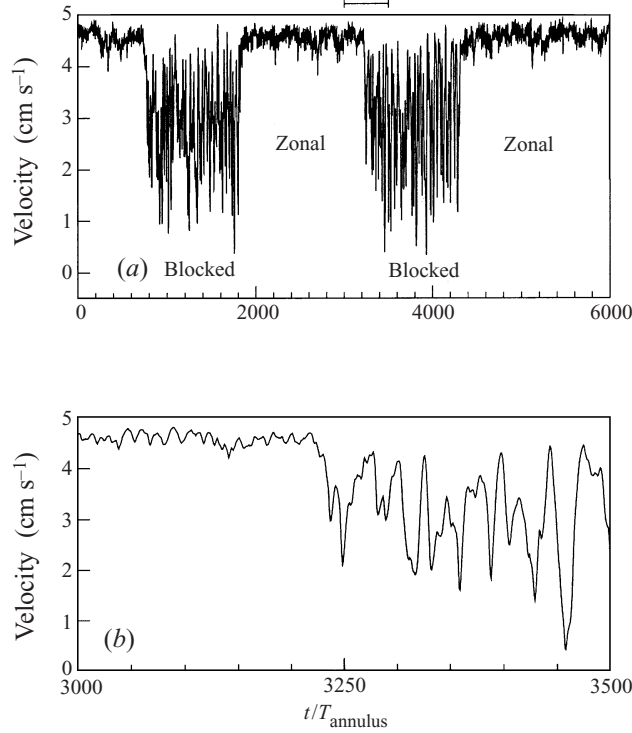


FIGURE 8. Spontaneous transitions between the two flow states, as seen in the azimuthal velocity signal. The parameters  $Ro = 0.0475 \pm 0.001$  and  $Ek = 4.8 \times 10^{-4}$  are held fixed (rotation rate  $\Omega = 3\pi \text{ rad s}^{-1}$  and pump flux  $F = 280 \text{ cm}^3 \text{ s}^{-1}$ ). Part (b) shows an expanded view of one of the transitions from (a).

1979; Gill 1982; Pedlosky 1987), and  $\nu$  is the eddy coefficient of lateral viscosity that simulates the effect of the subgrid-scale motions on the flow (Smagorinsky 1963; Kraichnan 1976).

To non-dimensionalize (3.1) we introduce the scaled variables,

$$\left. \begin{aligned} x &= a_r L x', & y &= L y', & t &= a_r t' / f, \\ h &= H h', & \psi &= L^2 f \psi', & \psi_* &= L^2 f \psi_*', \\ v &= L^2 f v', \end{aligned} \right\} \quad (3.2)$$

where  $L$  is chosen as the length scale,  $1/f$  as the time scale, and  $Lf$  as the velocity scale, while  $a_r$  is the aspect ratio of the channel. This yields the non-dimensional equation, with the primes dropped for convenience,

$$\frac{\partial}{\partial t} (\nabla^2 \psi) + J(\psi, \nabla^2 \psi + h_m) + \beta \frac{\partial \psi}{\partial x} = -a_r \kappa \nabla^2 (\psi - \psi_*) + a_r \nu \nabla^4 (\psi - \psi_*). \quad (3.3)$$

The non-dimensional Laplacian operator in (3.3) is defined as

$$\nabla^2 \psi \equiv \left( \frac{\partial^2}{a_r^2 \partial x^2} + \frac{\partial^2}{\partial y^2} \right) \psi, \quad (3.4)$$

and the two non-dimensional parameters on the right-hand side are defined as

$$\beta = \frac{Ls}{H}, \quad \kappa = \frac{(2A\nu f)^{1/2}}{fH}. \quad (3.5)$$

Formally, the  $\kappa$  defined in (3.5) is related to the Ekman number defined for the experiment in §2 by  $\kappa^2 = Ek$ . The actual value of  $\kappa$ , however, is determined by the turbulent viscosity  $A_V$  in the boundary layer, which is a function of the flow, rather than by the kinematic viscosity  $\nu$ , which is intrinsic to the fluid (Gill 1982; Pedlosky 1987). Therefore,  $\kappa$  can only be determined empirically in our numerical calculations, and we use  $\kappa$ -values from 0.001 to 0.01, based on qualitative similarity of the flow dynamics with the tank experiments.

As the vorticity forcing  $\psi_*$  does not change with time, once  $\nu$ ,  $\psi_* = \psi_*(x, y)$ , and  $h = h(x, y)$  are specified, the dynamics described by (3.3) is completely determined by the two parameters  $\beta$  and  $\kappa$  and the initial streamfunction field  $\psi(x, y, 0)$ .

### 3.1.2. Numerical formulation

The model equation (3.3) is solved numerically in a straight and periodic channel, neglecting the curvature of the tank, with a dimensionless width of  $\pi$  between the two lateral boundaries and spatial period of  $a_r\pi$  in the zonal direction (Lorenz 1963; Charney & DeVore 1979; Ghil & Childress 1987, §§5.2 and 6.3). Free-slip boundary conditions are imposed on the two sidewalls.

We use a pseudospectral method with de-aliasing (e.g. Orszag 1971) for spatial discretization, and a second-order predictor–corrector scheme for time integration (Lorenz 1963). There are 32 spectral modes in each spatial direction, but the nonlinear terms are computed using  $64 \times 64$  modes before dealiasing. Different time-step sizes and numbers of spatial modes, as well as other time integration schemes, have been tested to ensure the accuracy and physical realism of the numerical results.

The model parameters are chosen to match the laboratory settings. The aspect ratio  $a_r$  is chosen as the ratio of the mid-channel perimeter to the wall-to-wall width of the annulus, which yields  $a_r = 5\pi/3$ . The length scale  $L$  is the same order as the azimuthal extent of either mountain, taken to be 28 cm;  $H = 18.7$  cm is the mean depth of the water in the tank. Hence we have, from (3.5),

$$\beta = \frac{Ls}{H} = \frac{28 \times 0.1}{18.7} = 0.15. \quad (3.6)$$

As mentioned in the previous subsection, the value of the Ekman friction coefficient  $\kappa$  is chosen so that the model dynamics is similar to that in the experiment, since the turbulent viscosity  $A_V$  cannot be determined directly from the experiment. Our range of  $\kappa$  from 0.001 to 0.01 corresponds approximately to a reasonable range of  $A_V$  from 0.001 to  $0.1 \text{ cm}^2 \text{ s}^{-1}$ . The value of the eddy viscosity  $\nu$  is determined by trial and error (McWilliams *et al.* 1981), and we found that  $10^{-6} < \nu < 10^{-4}$  is a reasonable range.

The topography and forcing in the numerical model are like those in the tank. Two symmetric Gaussian ridges are specified, as in (2.1), and we tested two non-dimensional heights of the mountains:  $h_0 = 0.1$ , which is about the same height as the experimental mountains, and  $h_0 = 0.15$ . The forcing by the fluid pumped through the two rings of holes in the tank is simulated in the barotropic model as vorticity forcing, based on the quasi-geostrophic relation between vertical velocity in the bottom boundary layer and the induced free-fluid vorticity (see Pedlosky 1987, figure 4.5.1 and equation (4.5.39)). We use this Ekman pumping relation in the form

$$w_*(x, y) = \left( \frac{A_V}{2f} \right)^{1/2} \nabla^2 \psi_*(x, y), \quad (3.7)$$

where  $w_*$  is the forced vertical velocity through the holes, and  $\psi_*(x, y)$  is the forcing vorticity.

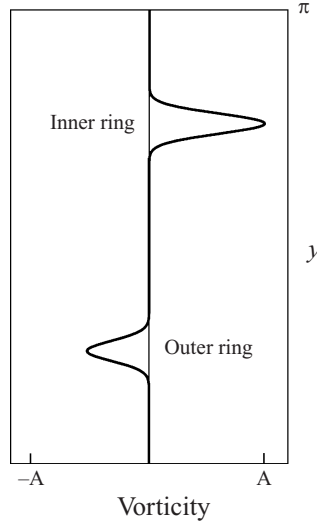


FIGURE 9. The cross-channel profile of the forcing vorticity in the numerical model. The width of the channel is  $\pi$ , while the simulated outer ring is located at  $y_1 = \pi/4$  and the inner ring at  $y_2 = 3\pi/4$ . The profile is given by (3.8) and the amplitude  $A$  is arbitrary.

Assuming  $w_*$  has a narrow Gaussian profile in the radial direction over either ring, we model the vorticity forcing as

$$\nabla^2 \psi_*(x, y) = A[\exp(-(y - y_2)^2/y_0^2) - (7/13)\exp(-(y - y_1)^2/y_0^2)]; \quad (3.8)$$

here  $A$  is the forcing amplitude, and  $y_0 = \pi/32$  is the e-folding width of the narrow  $w_*$  profile in the radial direction, with  $y_1 = \pi/4$  and  $y_2 = 3\pi/4$  being the position of the outer ring and inner ring, respectively. The value of  $y_0$  is chosen to be small enough to simulate the relative narrowness of the two rings in the annulus, while still large enough to have the forcing profile resolved by the numerical grid. The factor  $7/13$  comes from the fact that the averaged  $w_*$  along the outer ring is weaker than the inner ring because the outer ring has a longer perimeter, while the total water flux is the same through both. The vorticity forcing profile so obtained across the channel is shown in figure 9, with positive (negative) vorticity in the inner (outer) ring.

A Rossby number  $Ro$  of the forcing can be defined – independent of the flow details, as was done for the experiment – by integrating (3.8) over  $y$  to find the velocity profile, assuming axisymmetric flow and imposing a zero-slip boundary condition at  $y = 0$ . The exact form is complicated, but at  $y = \pi/2$  (the axis of the channel) the solution is approximately

$$U = \frac{1}{2}y_0\pi^{1/2}A, \quad (3.9)$$

with  $y_0 = \pi/32$  as discussed above. Due to the choice of non-dimensional units (see (3.2)),  $Ro = U$ ; for our value of  $y_0$  this simplifies to  $Ro \approx 0.017A$ .

### 3.2. Simulation results

#### 3.2.1. Blocked and zonal flows

The numerical model reproduces the blocked and zonal flows seen in the experiments, over a wide range of parameters. Figure 10 shows typical blocked and zonal flow patterns, projected from the model's straight-channel geometry to annular geom-

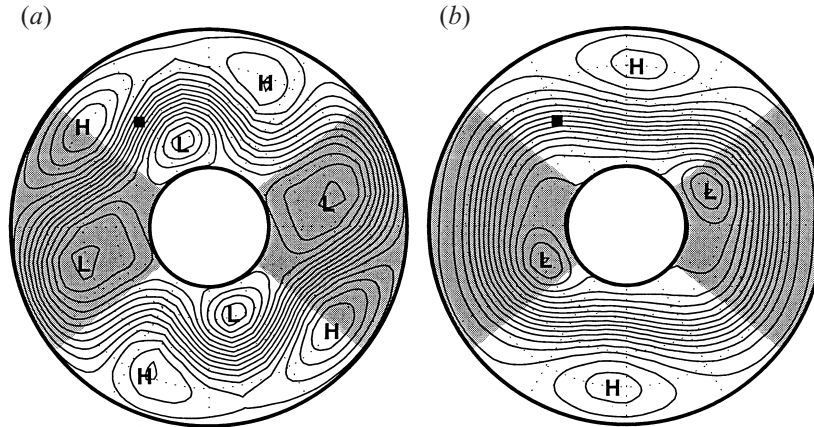


FIGURE 10. The time-averaged streamfunction field of the two types of flow seen in the numerical model, (a) blocked and (b) zonal. The parameters for the two cases are the same, with  $A = 2.0$ ,  $h_0 = 0.15$ ,  $\kappa = 0.01$ , and  $\nu = 5 \times 10^{-5}$ . The straight channel in the model is projected to the annular shape shown in the figure, with the shaded areas indicating the coverage of the mountains. Contour intervals: (a) 0.0125; (b) 0.025. The squares show the position of the simulated velocity probe. Compare these streamfunctions with those observed in the experiments (figure 2).

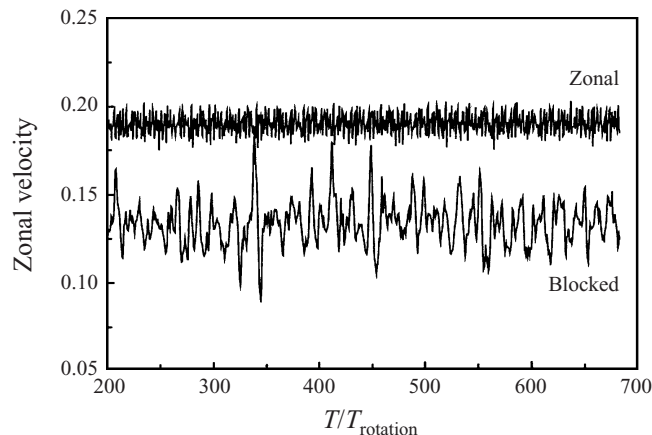


FIGURE 11. The non-dimensional zonal-velocity time series of the two flows in figure 10, measured at the position shown by the filled square, the same position as the hot-film probes in the tank. The azimuthal velocity of 0.20 is equivalent to a dimensional velocity of  $70 \text{ cm s}^{-1}$  at a tank rotation rate of  $\Omega = 2\pi \text{ rad s}^{-1}$ .

etry; this projection facilitates comparison with the laboratory experiments. Figure 11 shows the azimuthal velocity signals for the blocked and zonal flows.

The major features of the simulated blocked and zonal flows are qualitatively similar to their experimental counterparts. Both simulation (figure 10) and experiment (figure 2) show that the zonal flow has a strong jet with little meandering, and the associated cyclones near the inner wall lie over the downstream half of the topography. The zonal flows have small-amplitude, higher-frequency fluctuations in the jet velocity signal. Blocked flow in both simulation and experiment has a weak jet with pronounced meandering and two deep troughs on the downstream flank of the mountains. The blocked flows also have large-amplitude, low-frequency oscillations in the jet velocity, in both the experiment and the simulation (cf. figure 4a and

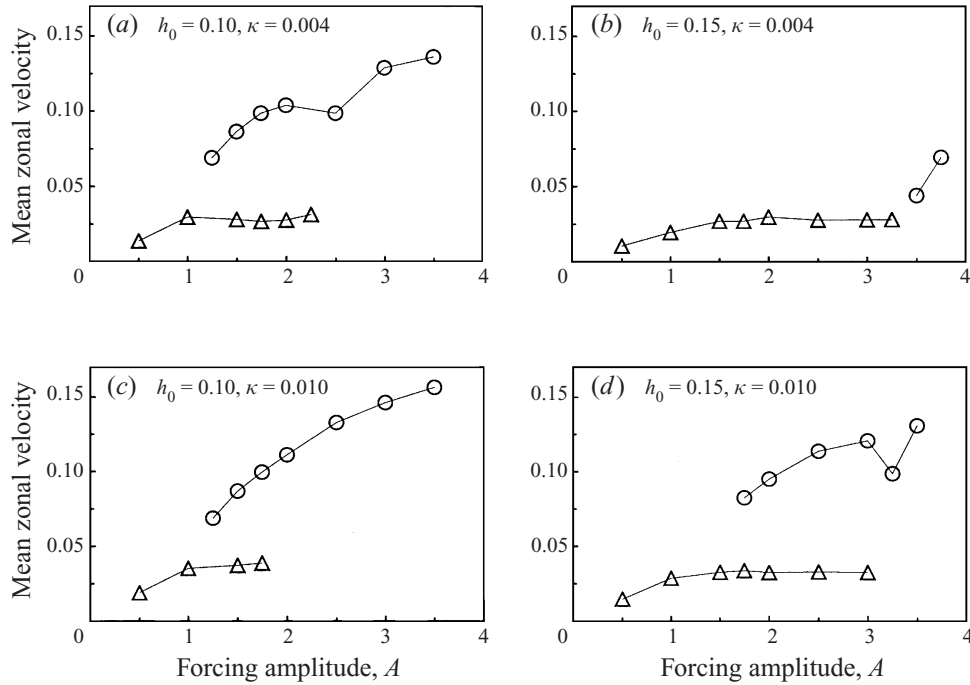


FIGURE 12. The time- and space-averaged azimuthal velocity as a function of the forcing amplitude  $A$ ,  $v = 5 \times 10^{-5}$ . (a–d) The results for the possible  $2 \times 2$  combinations of two topographic heights,  $h_0 = 0.10$  and  $h_0 = 0.15$ , and two Ekman friction values,  $\kappa = 0.004$  and  $\kappa = 0.01$ . The upper branch, indicated by circles, and the lower branch, indicated by triangles, are obtained from the zonal flows and blocked flows, respectively.

figure 11, respectively). The variance of the velocity time series with respect to its mean, however, is larger in the blocked experiment (figure 4a) than in the blocked simulation (figure 11).

The simulations allow us to resolve finer flow features than the experimental observations, as the latter are limited by the population of tracer particles and the resolution of the camera. For instance, the two zonally elongated anticyclones in the valleys, ‘equatorward’ of the jet in the zonal flow (figure 10b), are more clearly captured and appear to be more symmetric. It is also more obvious that each centre of the two secondary cyclones near the inner wall over the mountains is located downstream from the mountain’s ridge. Moreover, in the blocked flow (figure 10a), the two major anticyclones upstream of each mountain are stronger and better centred on the ‘western’ edge of the mountain, while the secondary highs about  $15^\circ$  downstream of each mountain’s ‘eastern’ edge are weaker than in the experiment (figure 2a) and are also more symmetric. In general, the appearance of a pronounced wavenumber-4 component in the blocked flow is clearer in the simulation.

### 3.2.2. Multiple equilibria

As in the laboratory study, for each selected set of control parameters, we start the numerical model with various initial states, in order to determine the number and the nature of the asymptotically stable states. Figure 12(a–d) shows four examples of the bifurcation diagrams so obtained. In each diagram, we plot the mean zonal velocity

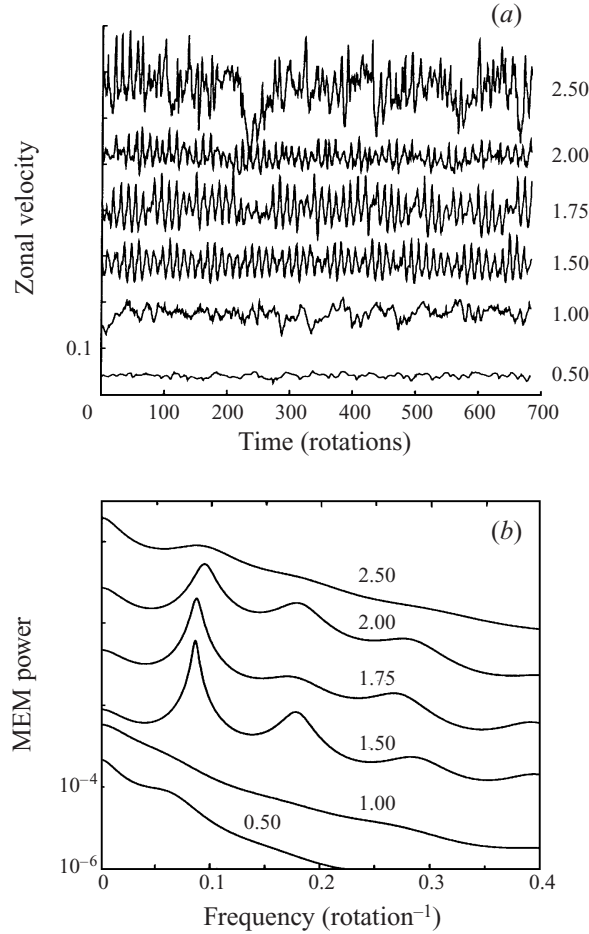


FIGURE 13. (a) Time series of the blocked-flow azimuthal velocity at the location of the simulated probe (see figure 10a), for various forcing amplitudes  $A$ , as labelled next to each curve. (b) Power spectra of the corresponding time series in (a), estimated using the maximum-entropy method. Other parameters:  $h_0 = 0.15$ ,  $\kappa = 0.006$ , and  $\nu = 5 \times 10^{-5}$ . All the curves in each panel are displayed on the same scale but displaced vertically to avoid overlapping.

of each stationary stable state reached by our model runs, averaged over the whole channel, as a function of the forcing amplitude  $A$ .

Both types of flow are present in all four cases, with zonal flows having a larger velocity than the blocked flows in each case. The mean zonal velocity of the zonal flows increases with the forcing amplitude, except for the minor ‘dips’ in figures 12(a) and 12(d), whereas in blocked flows the mean azimuthal velocity stays fairly flat after some initial increase while the forcing is still weak. In addition, zonal flows tend to exist over the higher range of the forcing, while blocked flows tend to be confined to the lower range. Both the maximal height of the topography  $h_0$  and the Ekman friction  $\kappa$  have a substantial influence on the stability of either flow. By increasing  $h_0$  or decreasing  $\kappa$ , blocked flow remains stable up to higher values of the forcing  $A$ , while by decreasing  $h_0$  or increasing  $\kappa$ , the stability of zonal flow at lower values of  $A$  is increased.

Furthermore, except in figure 12(b), there is a sizable range in the forcing amplitude in which stable zonal and blocked flows coexist. This indicates that the asymptotic

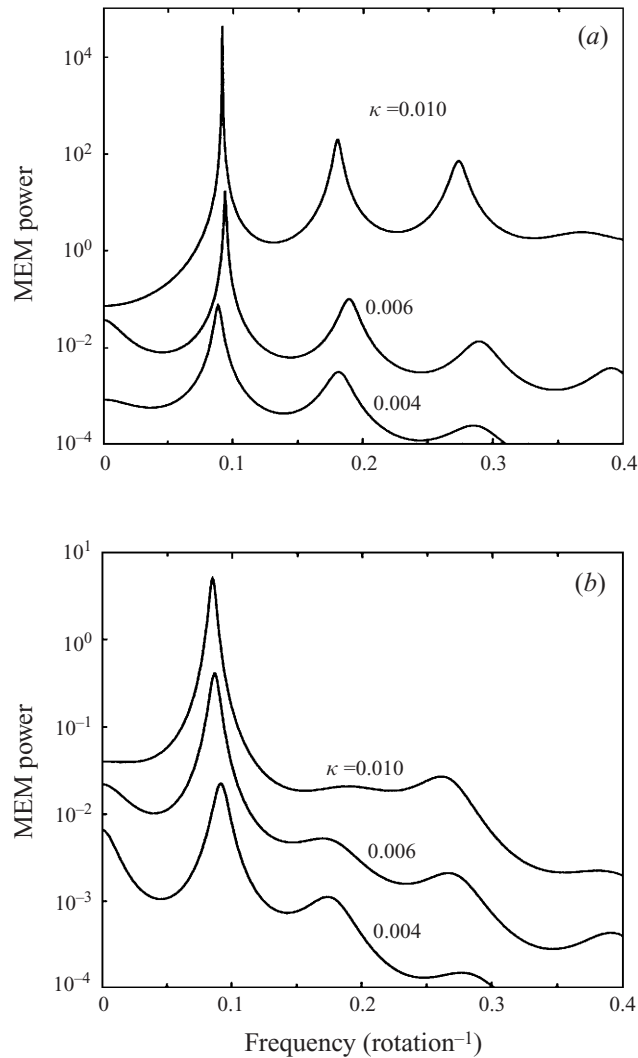


FIGURE 14. Maximum-entropy spectra of the zonal-velocity time series of the blocked flows for two mountain heights, (a)  $h_0 = 0.10$  and (b)  $h_0 = 0.15$ , and various values of Ekman friction  $\kappa$ . Forcing amplitude  $A = 1.75$  in both cases and  $\nu = 5 \times 10^{-5}$ . The curves are displayed on the same logarithmic scale but displaced vertically to avoid overlapping.

state reached by the flow does depend on the initial state, and multiple equilibria do exist for a wide range of parameter values (cf. figure 12*a, c, d*).

The pseudo-arclength continuation code described in Appendix B of Tian (1999) was applied to a number of preliminary versions of the model. It gave in all cases S-shaped bifurcation curves for the jet's intensity that resemble figure 6.5 of Ghil & Childress (1987), with zonal flows on the upper branch and blocked flows on the lower branch. This suggests that for the model version analysed in detail here, the multiple equilibria are due to back-to-back saddle-node bifurcations.

### 3.2.3. Low-frequency oscillations of blocked flows

We have examined the effect of forcing, topographic height, and Ekman friction on the blocked-flow low-frequency oscillations. Figure 13 shows velocity time series and

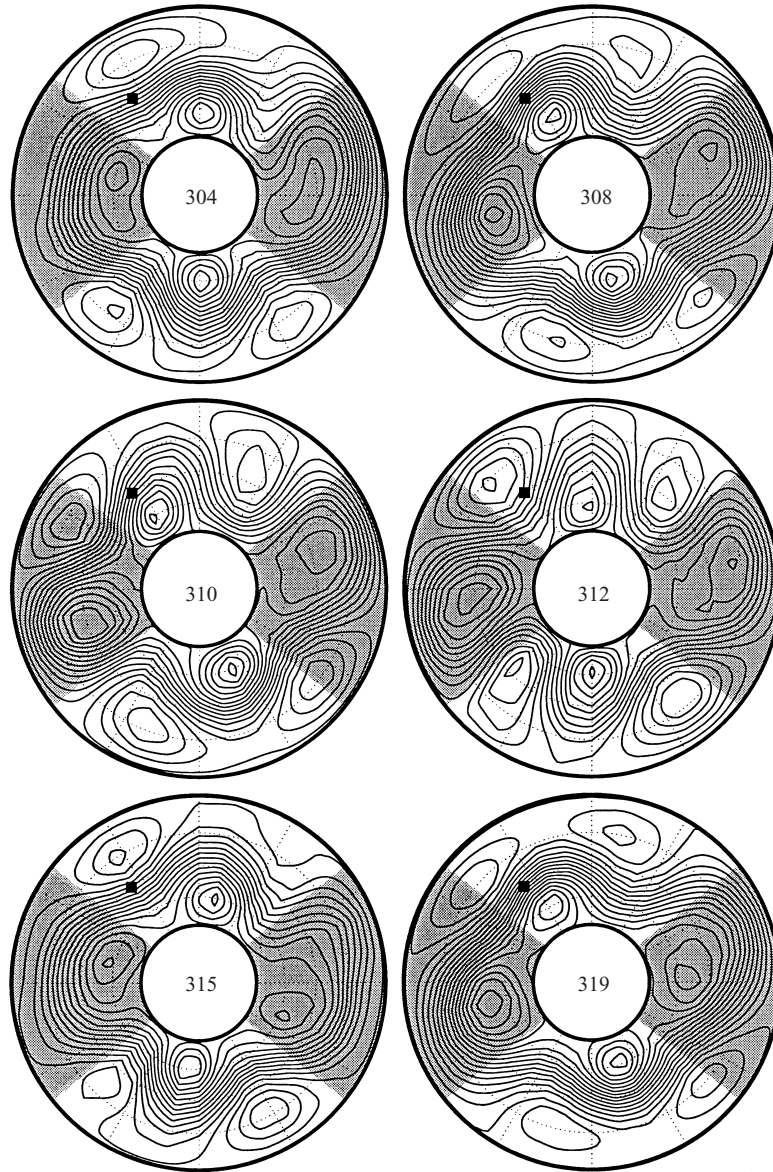


FIGURE 15. A sequence of snapshots of a numerically simulated blocked flow, showing the dynamics of the oscillations. The number in the centre of each frame is the time stamp in rotation periods, or 'days'.  $A = 1.75$ ,  $h_0 = 0.15$ ,  $\kappa = 0.006$ , and  $\nu = 5 \times 10^{-5}$ ; contour interval is 0.0125.

their power spectra for six values of the forcing amplitude  $A$ . At low  $A$ -values ( $A = 0.5$  and 1.0), the oscillations are quite weak. For intermediate values of  $A$ , the oscillations are stronger and fairly regular, with a period around 14 annulus rotations. At higher  $A$ -values ( $A = 2.5$ ), the velocity has very energetic and irregular fluctuations.

To illustrate the influence of the topographic height  $h_0$  and the Ekman friction  $\kappa$ , we show in figure 14 the power spectra of the low-frequency oscillations obtained with two different topographic heights (figure 14*a, b*) and three different values of  $\kappa$ . All the spectra in both panels have a peak corresponding roughly to a period of 12

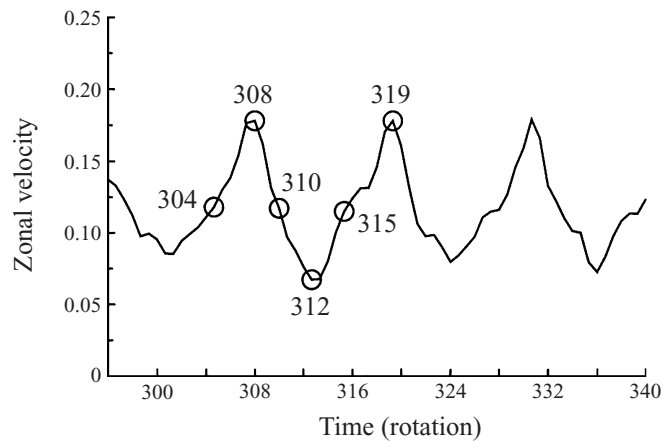


FIGURE 16. The azimuthal velocity measured at the probe position (square in figure 10a), including the time interval over which the oscillations are shown in figure 15. The six time stamps on the curve correspond to the six frames shown in figure 15.

annulus rotations. However, the spectra in figure 14(a), for lower mountains, have a sharper peak near this period than those in figure 14(b); thus the oscillations in the lower-mountain case tend to be more regular. Increasing the Ekman friction  $\kappa$  sharpens the peaks in either case, but does not change their location very much.

The blocked flows' oscillatory instability and its parameter dependence have been studied by Jin & Ghil (1990) in an analytic, weakly nonlinear model and by Strong *et al.* (1993, 1995) and Keppenne *et al.* (2000) in numerical models. The oscillations' main mechanism is the topographic modulation of the interaction between the stationary wave, whose ridge lies upstream of the topographic ridge, and the zonal flow. Oscillations in the wave's amplitude and the zonal position of its ridge are accompanied by oscillations in the torque that wave exerts on the mountains; the latter oscillations are counterbalanced by oscillations of the opposite sign in the torque exerted by the zonal flow's varying intensity. The sharper peaks obtained at the main period in the experiment for lower topography and stronger Ekman dissipation are consistent with the nonlinear effects decreasing with smaller  $h_0$  and larger  $\kappa$ .

To verify the main features of the blocked-flow oscillations—as described in the above-cited earlier work—we show a sequence of snapshots of the streamfunction field in figure 15. The six frames in the sequence correspond to slightly more than one cycle, with an approximate  $90^\circ$  phase difference between two consecutive frames. The exact phase of each frame is shown on the velocity signal for the same numerical run, displayed in figure 16.

The low-frequency oscillations in the strength and length of the jet are accompanied by changes in the shape, intensity and azimuthal position of the cyclonic and anticyclonic vortices, as well as by exchanges of kinetic energy between the jet and the vortices. They have the character of relaxation oscillations, already attributed by Namias (1950) to the atmospheric index cycle: the kinetic energy of the jet grows slowly (through roughly 7 rotations) and is discharged rapidly (over about 4 rotations) into the vortices (see figures 15 and 16). These oscillations are close to periodic, but not perfectly regular.

The flow fields in figure 15 are dominated by components of zonal wavenumber-2 and their harmonics of wavenumber-4, which confirms the controlling role of the topography. On the other hand, the flow fields are not perfectly symmetric with

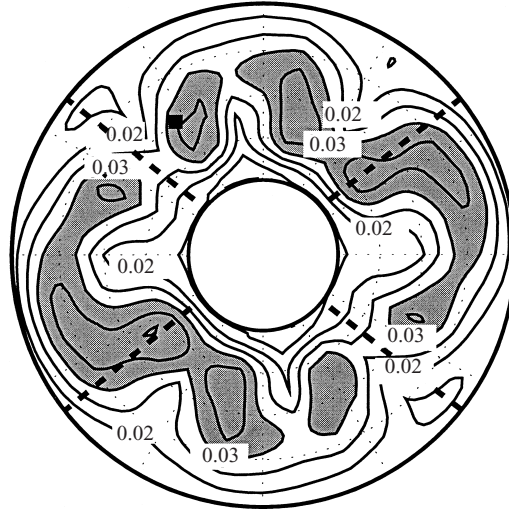


FIGURE 17. Variance of the streamfunction field of the blocked flow shown in figure 15. The dashed lines indicate the edges of the mountains. Contour interval: 0.005, with regions larger than 0.03 shaded.

respect to a shift by  $a_r\pi/2$ , the half-length of the channel, in the zonal direction; this implies that odd wave components are present, due to their nonlinear interaction with the topography (Tian 1997).

To see the spatial distribution of the oscillation's variability, we calculated the variance of the streamfunction of the flow shown in figure 15 over a long time interval. The result is displayed in figure 17, with the areas of largest variability shaded. These areas are located roughly along the path of the jet, especially where it runs around the deep troughs over the mountains, and over the secondary cyclones between the mountains. The largest area of strong variability covers the downstream flank of each deep trough; a smaller area with the same amplitude of variability is found on the upstream side of each secondary cyclone. The centres of the troughs and cyclones, however, exhibit very little variability, and so do the regions near the two sidewalls.

#### 3.2.4. Oscillations in the zonal flows

The small-amplitude fluctuations in the zonal flows (see figure 11) were also studied in the numerical model. Figure 18 shows the azimuthal velocity time series and the corresponding power spectra for six different values of the forcing amplitude. The amplitude of the oscillations (see panel *a*) increases as the forcing increases. The spectra (see panel *b*) reveal that each oscillation has a dominant frequency, accompanied by several harmonics or subharmonics. These secondary frequencies are regularly distributed and occupy much of the range of 1 to 10 rotation periods, with various amplitudes relative to the dominant peak. No systematic change in the location and amplitude of the dominant frequency, nor in the relative amplitude of the secondary frequencies can be observed as the forcing increases. The frequencies are all, however, higher than those that characterize the blocked-flow oscillations.

Inspection of the flow fields (not shown) indicates that these oscillations in the jet velocity are mainly induced by the slight libration movement of the two secondary cyclones. Located on the inner-wall side of the jet and close to the wall, these cyclones appear to be driven by the shear between the jet and the wall. They move back and

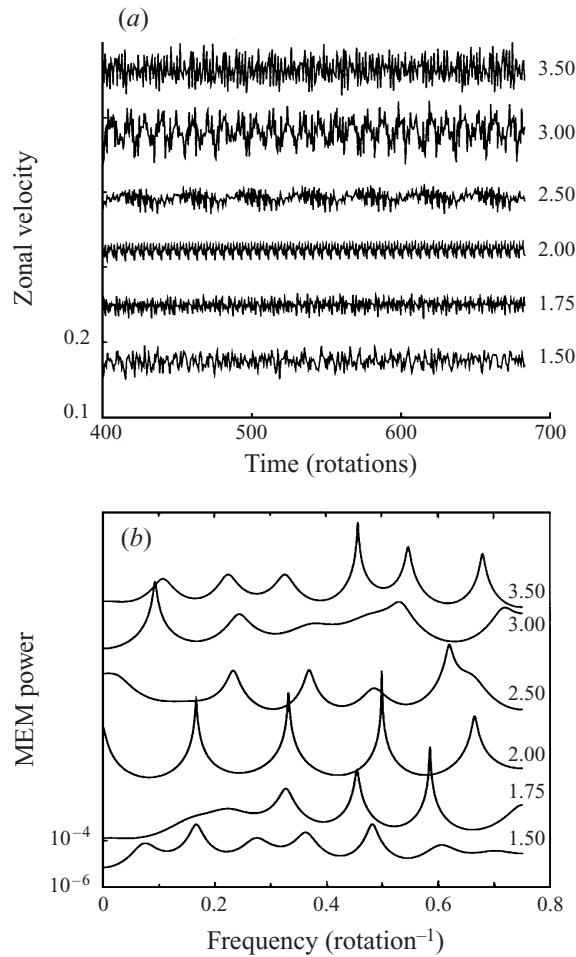


FIGURE 18. (a) Time series and (b) maximum-entropy spectra of the azimuthal velocity time series measured at the probe position in the zonal flows. The numbers on each curve are the forcing amplitude  $A$ ;  $h_0 = 0.10$ ,  $\kappa = 0.01$ , and  $\nu = 5 \times 10^{-5}$ . The curves are displaced vertically to avoid overlapping.

forth slightly—with some change in intensity but without significant effect on the shape of the jet—over the downstream flank of the two mountains.

## 4. Summary and discussion

### 4.1. Comparison between laboratory and numerical results

In laboratory experiments on a barotropic rotating annulus with two symmetric, Gaussian-shaped mountains as the bottom topography (figure 1), two distinct flow patterns were obtained. One of them resembles atmospheric high-index or zonal flows, the other low-index or blocked flows in the atmosphere (see figure 2). The phase relations between the main flow features and the topography, as well as the corresponding azimuthal velocity of the jet, show that topographic resonance affects the flows: the zonal flows appear super-resonant, while the blocked flows appear to be subresonant. The jet velocity of zonal flow is higher than the critical velocity for linear

resonance of Rossby waves with the topography, while the jet velocity of blocked flow is lower than this resonant velocity (figure 4). The important role of the topography is also seen from the dominance of zonal wavenumber-2 in both zonal and blocked flows, and the flow patterns' nearly fixed position relative to the mountains.

Blocked flows are stable at low  $Ro$  and  $Ek$ . Between the two regimes in parameter space where either flow is stable lies a region where the flow switches intermittently from one flow pattern to the other (see figure 7).

Essentially the same flow patterns, zonal and blocked, were obtained in a numerical model designed to simulate the flow in the rotating annulus. However, quantitative comparison is not possible because the numerical model's parameters  $A$  and  $\kappa$  cannot be determined directly from the experiment. Further, the simulation neglects sidewall and curvature effects. Nevertheless, the two types of flow regimes in the model, zonal and blocked, have much the same spatial and temporal characteristics as their counterparts in the experiment. These common characteristics include the shape and position of the cyclonic and anticyclonic vortices in the flow (compare figure 2 and figure 10), the strength and configuration of the jet, the large-amplitude low-frequency oscillations associated with the blocked flows, and the small-amplitude fluctuations associated with the zonal flows (compare figure 4 and figure 11).

In the numerical model, multiple equilibria exist for a wide range of parameters (figure 12). Higher mountains lead to stronger nonlinear interactions between the mountains and the flow and, when the flow is stabilized by sufficient Ekman friction, there is a rather large region in which the two flow patterns coexist as stable equilibria (see figure 12*d*). This is in contrast to the laboratory experiments, where no multiple equilibria were observed. Instead, at moderate  $Ro$  both flows in the rotating annulus are metastable, and spontaneous transitions between the two take place abruptly and at irregular intervals.

Two-way spontaneous transitions between the zonal and blocked flows have not been found in the numerical model. Since there is a certain amount of noise in the tank's forcing,  $O(1 \text{ cm}^3 \text{ s}^{-1})$ , we tried adding white noise to the forcing in the numerical model; even when the noise was fairly strong, however, no transitions were observed. Furthermore, as the Ekman friction is a function of the flow instead of the fluid, we tested various parameterization schemes (e.g. Gill 1982, Chap. 9; Stull 1988, Chap. 6) to relate the friction with the properties of the flow, such as the velocity or kinetic energy. Various schemes had different effects on the dynamics of the flow, but did not result in spontaneous transitions. A change in the forcing profile and a different formulation of the eddy viscosity term (Treguier & McWilliams 1990; Ghil & Paldor 1994) did not induce the transitions either. In a similar numerical model but with a different jet profile and simplified mountains (Tian 1997), no transitions were observed in spite of the existence of similar blocked and zonal flow states.

One possible explanation is that three-dimensional effects in the laboratory flows, not captured by our purely two-dimensional models, may have played an important role during the transition. We have observed during the transition that the large-scale coherent structure of either flow pattern, zonal or blocked, first breaks into smaller-scale, turbulent flows, and then reorganizes itself into the other metastable flow pattern. Moreover, zonal flows have several times as much kinetic energy as the blocked ones and, during the short transition interval to blocked flow, a considerable amount of kinetic energy must be dissipated. Small-scale three-dimensional turbulent flow features would help dissipate this energy.

We tried to test this hypothesis by examining the velocity records from the top and bottom hot-film probes, for indications of loss of correlation during the transitions.

The rapidity of the transitions, however, makes it difficult to determine whether the velocities at the tank's top and bottom become uncorrelated during a transition. Further studies are needed on the detailed physical processes that operate during the transitions. This will require a model with three-dimensional dynamics and possibly higher horizontal resolution.

The azimuthal velocity in the numerical model's blocked flows is typically about  $35 \text{ cm s}^{-1}$ , which is larger than that obtained for similar conditions in the experiments; the latter is usually less than  $20 \text{ cm s}^{-1}$ . We speculate that the disagreement is due to two reasons. One is that we used a continuous band of forcing vorticity along the channel in the numerical model, rather than 120 small discrete holes as in the experiment. The former is much more efficient in forcing the jet. The other is the absence of friction from the two sidewalls in the numerical model, in which we imposed free-slip boundary conditions. This friction, though less effective than the Ekman friction in the top and bottom layers, may damp the jet velocity and lower the frequency of the oscillations. The presence of the lateral boundaries might also play a role in the three-dimensional flow effects mentioned in the previous paragraph.

#### 4.2. Connections to the atmosphere

The two types of flows we obtained in the tank and in the model are qualitatively similar to high- and low-index, or zonal and blocked flows in the atmosphere. Still, the atmosphere's large-scale persistent flow patterns are clearly more complicated. In spite of the complexity of ever-changing weather patterns and the shortness of instrumental records, observational studies have determined that multiple regimes can be identified (Cheng & Wallace 1993; Kimoto & Ghil 1993*a, b*; Michelangeli, Vautard & Legras 1995). More precise relationships between the two types of flow found here, experimentally and numerically, and the flow regimes in the Northern Hemisphere's atmosphere remain to be determined. This task is rendered more difficult by the fact that—in spite of recent progress in this direction—there is still no consensus on the exact number and flow patterns of the Northern Hemisphere's flow regimes.

Cheng & Wallace (1993), Kimoto & Ghil (1993*a*), Smyth, Ide & Ghil (1999), and Corti, Molteni & Palmer (1999) all essentially find two regimes, zonal and blocked, in each one of the Pacific/North-American and Atlantic–European sectors of the hemisphere. But Kimoto & Ghil (1993*b*), Michelangeli *et al.* (1995) and Robertson & Ghil (1999), among others, each find slightly larger numbers of regimes in one or the other of the sectors, or both. The latter represent a finer subdivision of the two regimes, zonal and blocked, obtained by the 'conservative' or 'parsimonious' classification of the former set of authors. This subdivision in the 'richer classifications' might correspond to an identification as separate regimes of slow phases of an oscillation about blocked flow like the one described here in some detail. It might correspond, on the other hand, to the existence of regimes that have distinct physical origins but, being more sparsely populated (at least over the last half-century of instrumental upper-air data), get lumped into a single regime by the more conservative classification methods.

Although our original motivation for these investigations arose from the multiple regimes and intraseasonal oscillations that contribute to the atmosphere's low-frequency variability, we do not expect to obtain straightforward answers to the questions raised by the real atmosphere from the results obtained in our idealized rotating annulus and numerical models. Nevertheless, explorations like those reported here do provide insight into the fundamental dynamics, and suggest guidelines for analysis of the atmospheric observations.

Oscillations are present in zonal and blocked flows in both the annulus and the

atmosphere. In the atmosphere, the oscillations about zonal flows arise mainly from baroclinic instability, not present in our barotropic annulus and model. The low-frequency oscillations about the blocked flows in our study, however, are more likely to have common features with the observed ones (see Ghil & Robertson 2000 for a recent review of work on intraseasonal oscillations in the Northern Hemisphere extratropics). The description and energy diagnostics of the oscillations here can thus help prove or disprove a topographic origin for the atmospheric oscillations.

We thank P. Billant, M. Kimoto, L. Panetta, B. Plapp, and D. J. Tritton (deceased; see H. L. Swinney & P. A. Davies, *Phys. Today* vol. 52 (1999), p. 82) for helpful discussions. Constructive comments from five anonymous reviewers greatly improved the presentation. The laboratory experiments (E. R. W., J. S. U., C. N. B., H. L. S.) were supported by the Office of Naval Research and the numerical studies were supported by NASA grant NAG 5-9294 (K. I. and Y. T.) and by an NSF Special Creativity Award (M. G.). M. G. furthermore thanks his hosts at the Ecole Normale Supérieure in Paris for their hospitality during the sabbatical that helped complete this work. This is publication number 5483 of UCLA's Institute of Geophysics and Planetary Physics.

## REFERENCES

- ANDERSON, J. R. & ROSEN, R. D. 1983 The latitude-height structure of 40–50 day variations in atmospheric angular momentum. *J. Atmos. Sci.* **40**, 1584–1591.
- BERNARDET, P., BUTET, A., DÉQUÉ, M., GHIL, M. & PFEFFER, R. L. 1990 Low-frequency oscillations in a rotating annulus with topography. *J. Atmos. Sci.* **47**, 3023–3043.
- BOLIN, B. 1950 On the influence of the earth's orography on the general character of the westlies. *Tellus* **2**, 184–195.
- CARNEVALE, G. F., KLOOSTERZIEL, R. C. & HEIJST, G. J. F. VAN 1991 Propagation of barotropic vortices over topography in a rotating tank. *J. Fluid Mech.* **233**, 119–139.
- CHARNEY, J. G. & DEVORE, J. G. 1979 Multiple flow equilibria in the atmosphere and blocking. *J. Atmos. Sci.* **36**, 1205–1216.
- CHARNEY, J. G. & ELIASSEN, A. 1949 A numerical method for predicting the perturbations of the middle latitude westerlies. *Tellus* **1**, 38–54.
- CHARNEY, J. G., SHUKLA, J. & MO, K. C. 1981 Comparison of a barotropic blocking theory with observation. *J. Atmos. Sci.* **38**, 762–779.
- CHARNEY, J. G. & STRAUS, D. M. 1980 Form-drag instability, multiple equilibria and propagating planetary waves in baroclinic, orographically forced, planetary wave systems. *J. Atmos. Sci.* **37**, 1157–1176.
- CHENG, X. & WALLACE, J. M. 1993 Cluster analysis of the Northern Hemisphere wintertime 500-hpa height field spatial patterns. *J. Atmos. Sci.* **50**, 2674–2696.
- CORTI, S., MOLteni, F. & PALMER, T. N. 1999 Signature of recent climate change in frequencies of natural atmospheric circulation regimes. *Nature* **398**, 799–802.
- DETINGER, M. D., GHIL, M., STRONG, C. M., WEIBEL, W. & YIOU, P. 1995 Software expedites singular-spectrum analysis of noisy time series. *EOS, Trans. AGU* **76**, 14–21 (see also <http://www.atmos.ucla.edu/tcd/>).
- DICKEY, J. O., GHIL, M. & MARCUS, S. L. 1991 Extratropical aspects of the 40–50 day oscillation in length-of-day and atmospheric angular momentum. *J. Geophys. Res.* **96**, 22643–22658.
- DOLE, R. M. & GORDON, N. D. 1983 Persistent anomalies of the extratropical Northern Hemisphere winter time circulation: Geographical distribution and regional persistence characteristics. *Mon. Wea. Rev.* **111**, 1567–86.
- DOWLING, T. E. & INGERSOLL, A. P. 1989 Jupiter's Great Red Spot as a shallow water system. *J. Atmos. Sci.* **46**, 3256–3278.
- EGGER, J. 1978 Dynamics of blocking highs. *J. Atmos. Sci.* **35**, 1788–1801.
- GHIL, M. 1987 Dynamics, statistics, and predictability of planetary flow regimes. In *Irreversible*

- Phenomena and Dynamical Systems Analysis in the Geosciences* (ed. C. Nicolis & G. Nicolis), pp. 241–283. Reidel.
- GHIL, M. & CHILDRESS, S. 1987 *Topics in Geophysical Fluid Dynamics Atmospheric Dynamics, Dynamo Theory, and Climate Dynamics*. Springer.
- GHIL, M. & MO, K. 1991 Intraseasonal oscillations in the global atmosphere. Part I. Northern Hemisphere and tropics. *J. Atmos. Sci.* **48**, 752–779.
- GHIL, M. & PALDOR, N. 1994 A model equation for nonlinear wavelength selection and amplitude evolution of frontal waves. *J. Nonlin. Sci.* **4**, 471–96.
- GHIL, M. & ROBERTSON, A. W. 2000 Solving problems with GCMs: General circulation models and their role in the climate modeling hierarchy. In *General Circulation Model Development: Past, Present, and Future* (ed. D. Randall), pp. 285–325. Academic.
- GILL, A. E. 1982 *Atmosphere–Ocean Dynamics*. Academic.
- GREENSPAN, H. P. 1968 *The Theory of Rotating Fluids*. Cambridge.
- HART, J. E. 1979 Barotropic quasi-geostrophic flow over anisotropic mountains. *J. Atmos. Sci.* **36**, 1736–1746.
- HELD, I. M. 1983 Stationary and quasi-stationary eddies in the extratropical troposphere: theory. In *Large-Scale Dynamical Processes in the Atmosphere* (ed. B. J. Hoskins & R. P. Pearce), pp. 127–169. Academic.
- HOLLOWAY, G. 1992 Representing topographic stress for large-scale ocean models. *J. Phys. Oceanogr.* **22**, 1033–1046.
- JIN, F.-F. & GHIL, M. 1990 Intraseasonal oscillations in the extratropics: Hopf bifurcation and topographic instabilities. *J. Atmos. Sci.* **47**, 3007–3022.
- JONAS, P. R. 1981 Laboratory observations of the effects of topography on baroclinic instability. *Q. J. R. Met. Soc.* **107**, 775–792.
- KEPPENNE, C. L. & INGERSOLL, A. P. 1995 High-frequency orographically forced variability in a single-layer model of the Martian atmosphere. *J. Atmos. Sci.* **52**, 1949–1958.
- KEPPENNE, C. L., MARCUS, S., KIMOTO, M. & GHIL, M. 2000 Intraseasonal variability in a two-layer model and observations. *J. Atmos. Sci.* **57**, 1010–1028.
- KIMOTO, M. & GHIL, M. 1993*a* Multiple flow regimes in the Northern Hemisphere winter. Part I. Methodology and hemispheric regimes. *J. Atmos. Sci.* **50**, 2625–2643.
- KIMOTO, M. & GHIL, M. 1993*b* Multiple flow regimes in the Northern Hemisphere winter. Part II. Sectorial regimes and preferred transitions. *J. Atmos. Sci.* **50**, 2645–2673.
- KRAICHNAN, R. H. 1976 Eddy viscosity in two and three dimensions. *J. Atmos. Sci.* **33**, 1521–1536.
- LANGLEY, R. B., KING, R. W. & SHAPIRO, I. I. 1981 Atmospheric angular momentum and the length of day: a common fluctuation with a period near 50 days. *Nature* **294**, 730–732.
- LAU, N. C. & NATH, M. J. 1987 Frequency dependence of the structure and temporal development of wintertime tropospheric fluctuations: comparison of a GCM simulation with observations. *Mon. Wea. Rev.* **115**, 251–271.
- LEGRAS, B. & GHIL, M. 1985 Persistent anomalies, blocking, and variations in atmospheric predictability. *J. Atmos. Sci.* **42**, 433–471.
- LI, G.-Q., KUNG, R. & PFEFFER, R. L. 1986 An experimental study of baroclinic flows with and without two-wave bottom topography. *J. Atmos. Sci.* **43**, 2585–2599.
- LORENZ, E. N. 1963 The mechanics of vacillation. *J. Atmos. Sci.* **20**, 448–464.
- LORENZ, E. N. 1972 Barotropic instability of Rossby wave motion. *J. Atmos. Sci.* **29**, 258–264.
- LOTT, F., ROBERTSON, A. W. & GHIL, M. 2001 Mountain torques and atmospheric oscillations. *Geophys. Res. Lett.* **28**, 1207–1210.
- MADDEN, R. A. & JULIAN, P. R. 1971 Detection of a 40–50 day oscillation in the zonal wind in the tropical Pacific. *J. Atmos. Sci.* **28**, 702–708.
- MADDEN, R. A. & JULIAN, P. R. 1972 Description of global-scale circulation cells in the tropics with a 40–50 day period. *J. Atmos. Sci.* **29**, 1109–1123.
- MARCUS, P. S. & LEE, C. 1998 A model for eastward and westward jets in laboratory experiments and planetary atmospheres. *Phys. Fluids* **10**, 1474–1489.
- MARCUS, S. L., GHIL, M. & DICKEY, J. O. 1994 The extratropical 40-day oscillation in the UCLA general circulation model. Part I. Atmospheric angular momentum. *J. Atmos. Sci.* **51**, 1431–1446.
- MARCUS, S. L., GHIL, M. & DICKEY, J. O. 1996 The extratropical 40-day oscillation in the UCLA general circulation model. Part II: Spatial structure. *J. Atmos. Sci.* **53**, 1993–2014.

- MCWILLIAMS, J. C., FLIERL, G. R., LARICHEV, V. D. & REZNIK, G. M. 1981 Numerical studies of barotropic modons. *Dyn. Atmos. Oceans* **5**, 219–238.
- MICHELANGELI, P.-A., VAUTARD, R. & LEGRAS, B. 1995 Weather regimes recurrence and quasi stationarity. *J. Atmos. Sci.* **52**, 1237–1256.
- NAMIAS, J. 1950 The index cycle and its role in the general circulation. *J. Met.* **7**, 130–139.
- O'CONNOR, J. F. 1963 The weather and circulation of January 1963. *Mon. Wea. Rev.* **91**, 209–218.
- ORSZAG, S. A. 1971 Galerkin approximations to flows within slabs, spheres, and cylinders. *Phys. Rev. Lett.* **26**, 1100–1103.
- PEDLOSKY, J. 1981 Resonant topographic waves in barotropic and baroclinic flows. *J. Atmos. Sci.* **38**, 2626–2641.
- PEDLOSKY, J. 1987 *Geophysical Fluid Dynamics*, 2nd edn. Springer.
- PEIXOTO, J. P., SALTZMAN, B. & TEWELES, S. 1964 Harmonic analysis of the topography along parallels of the earth. *J. Geophys. Res.* **69**, 1501–1505.
- PERVEZ, M. S. & SOLOMON, T. H. 1994 Long-term tracking of neutrally buoyant tracer particles in two-dimensional fluid flows. *Exps. Fluids* **17**, 135–140.
- PFEFFER, R. L., AHLQUIST, J., KUNG, R. & CHANG, Y. 1990 A study of baroclinic wave behavior over bottom topography using complex principal component analysis of experimental data. *J. Atmos. Sci.* **47**, 67–81.
- PFEFFER, R. L. & CHIANG, Y. 1967 Two kinds of vacillation in rotating laboratory experiments. *Mon. Wea. Rev.* **95**, 75–82.
- PFEFFER, R. L., KUNG, R., DING, W. & LI, G. Q. 1993 Barotropic flow over bottom topography-experiments and nonlinear theory. *Dyn. Atmos. Oceans* **19**, 101–114.
- PFEFFER, R. L., KUNG, R. & LI, G. Q. 1989 Topographically forced waves in a thermally driven rotating annulus of fluid-experiment and linear theory. *J. Atmos. Sci.* **46**, 2331–2343.
- PRATTE, J. M. & HART, J. E. 1991 Experiments on periodically forced flow over topography in a rotating fluid. *J. Fluid Mech.* **229**, 87–114.
- QUENEY, P. 1947 *Theory of Perturbations in Stratified Currents with Applications to Air Flow over Mountain Barriers*. University of Chicago Press.
- REX, D. F. 1950a Blocking action in the middle troposphere and its effect upon regional climate. I. An aerological study of blocking action. *Tellus* **2**, 196–211.
- REX, D. F. 1950b The climatology of blocking action. *Tellus* **2**, 275–301.
- ROBERTSON, A. W. & GHIL, M. 1999 Large-scale weather regimes and local climate over the western United States. *J. Climate* **12**, 1796–1813.
- ROSSBY, C. G. (and collaborators) 1939 Relation between variations in the intensity of the zonal circulation of the atmosphere and the displacements of the semi-permanent centers of action. *J. Mar. Res.* **2**, 38–55.
- SMAGORINSKY, J. 1963 General circulation experiments with the primitive equations. I. The basic experiment. *Mon. Wea. Rev.* **91**, 99–164.
- SMITH, R. B. 1989 Hydrostatic air-flow over mountains. *Adv. Geophys.* **31**, 1–41.
- SMYTH, P., IDE, K. & GHIL, M. 1999 Multiple regimes in Northern Hemisphere height fields via mixture model clustering. *J. Atmos. Sci.* **56**, 3704–3723.
- SOLOMON, T. H., HOLLOWAY, W. J. & SWINNEY, H. L. 1993 Shear flow instabilities and Rossby waves in barotropic flow in a rotating annulus. *Phys. Fluids A* **5**, 1971–1982.
- SOMMERIA, J., MEYERS, S. D. & SWINNEY, H. L. 1989 Laboratory model of a planetary eastward jet. *Nature* **337**, 58–61.
- SOMMERIA, J., MEYERS, S. D. & SWINNEY, H. L. 1991 Experiments on vortices and Rossby waves in eastward and westward jets. In *Nonlinear Topics in Ocean Physics* (ed. A. R. Osborne), pp. 227–269. North-Holland.
- STRONG, C. M., JIN, F.-F. & GHIL, M. 1993 Intraseasonal variability in a barotropic model with seasonal forcing. *J. Atmos. Sci.* **50**, 2965–2986.
- STRONG, C. M., JIN, F.-F. & GHIL, M. 1995 Intraseasonal oscillations in a barotropic model with annual cycle, and their predictability. *J. Atmos. Sci.* **52**, 2627–2642.
- STULL, R. B. 1988 *An Introduction to Boundary Layer Meteorology*. Kluwer.
- TIAN, Y. 1997 Eastward jet over topography: Experimental and numerical investigations. MS thesis, University of California, Los Angeles.

- TIAN, Y. 1999 Atmospheric intraseasonal variability: Observational, numerical and laboratory studies. PhD thesis, University of California, Los Angeles.
- TREGUIER, A. M. & MCWILLIAMS, J. C. 1990 Topographic influences on wind-driven, stratified flow in a beta-plane channel: An idealized model for the Antarctic Circumpolar Current. *J. Phys. Oceanogr.* **20**, 321–343.
- WALLACE, J. M. & BLACKMON, M. L. 1983 Observations of low-frequency variability. In *Large-Scale Dynamical Processes in the Atmosphere* (ed. B. J. Hoskins & R. P. Pearce), pp. 55–93. Academic.
- WEBSTER, P. J. & KELLER, J. L. 1975 Atmospheric variations: Vacillations and index cycles. *J. Atmos. Sci.* **32**, 1283–1300.
- WEEKS, E. R., TIAN, Y., URBACH, J. S., IDE, K., SWINNEY, H. L. & GHIL, M. 1997 Transitions between blocked and zonal flows in a rotating annulus with topography. *Science* **278**, 1598–1601.
- WURTELE, M. G., SHARMAN, R. D. & DATTA, A. 1996 Atmospheric lee waves. *Ann. Rev. Fluid Mech.* **28**, 429–476.
- YODEN, S. 1985 Bifurcation properties of a quasi-geostrophic, barotropic, low-order model with topography. *J. Met. Soc. Japan* **63**, 535–546.